Journal of Magnetic Resonance **137,** 108–115 (1999)
Article ID jmre.1998.1645, available online at http://www.idealibrary.com on IDEAL®

Mapping the B_1 Field Distribution with Nonideal Gradients in a High-Resolution NMR Spectrometer

Alexej Jerschow* and Geoffrey Bodenhausen*,†,[1]

*Section de Chime, Université de Lausanne, BCH, 1015 Lausanne, Switzerland; and †Département de chimie, Associé au CNRS, Ecole Normale Supérieure, 24 rue Lhomond, 75231 Paris cedex 05, France

Received June 8, 1998; revised October 14, 1998

To understand the behavior of many NMR experiments, it is important to determine the spatial distribution of the B_1 field. In this paper, we show how this distribution can be mapped independently of spin density, coil responsiveness, and nonlinearities of the B_0 field gradients. As a by-product we obtain a map of the (possibly nonlinear) spatial variation of the B_0 field gradients used in the imaging procedure. © 1999 Academic Press

Key Words: **B_1 field mapping; nonlinear B_0 gradients; coil responsiveness; calibration of nutation angles; edge effects.**

INTRODUCTION

In many cases, it is tacitly assumed in NMR that B_1 fields are homogeneous over the full volume of the sample. Only a few recent methods deliberately use inhomogeneous B_1 fields for the selection of coherence pathways (*1*), for spoiling transverse magnetization (*2*), for imaging (*3–7*), and for diffusion measurements (*8, 9*). These techniques have been recently reviewed by Canet (*10*). However, more often than not, nonuniform B_1 fields are regarded as a nuisance that merely leads to nonideal behavior. Very often, some sweeping assumptions are made about the B_1 field distribution, but uneducated guesses may lead to problems, in particular for experiments that involve two inhomogeneous rf fields B_{1I} and B_{1S} generated by two different transmitter coils. Indeed, the efficiency of experiments such as cross-polarization critically depends on the spatial correlation between these fields (*11*). In principle, the B_1 field distribution can be calculated theoretically if the coil geometry is known, or it can be mapped experimentally by moving a small sample across the volume of interest. In this paper we present a more direct approach, where B_1 field maps are obtained by imaging techniques. The methods are independent of the spatial distribution of the spin density, of the coil responsiveness, and of nonlinearities of the B_0 gradients that are used to obtain the image. This latter aspect is of particular importance in high-resolution probes with triple gradient coils. The spatial dependence of the B_0 fields created by nonideal gradients can also be obtained. Susceptibility changes over the sample volume can be neglected in homogeneous samples as used here. The use of strong B_0 gradients can help to avoid complications in inhomogeneous samples (*12*).

[1] To whom correspondence should be addressed. E-mail: Geoffrey.Bodenhausen@ens.fr.

THEORY

The simplest way to obtain an estimate of the inhomogeneity of the B_1 field is to perform a so-called *nutation experiment*, where a free induction decay (FID) is acquired after an rf pulse of variable duration. However, the decay constant of the envelope of the nutation signals only provides an estimate of the width ΔB_1 of the distribution of the rf field but not of the spatial dependence $B_1(x, y, z)$ of this field. To obtain such a function, it is necessary to turn to imaging experiments such as is shown in Fig. 1.

The three-dimensional echo recorded from the sequence in Fig. 1 is best described in **k**-space notation (*12*) with $\mathbf{k} = (k_x, k_y, k_z) = \gamma[G_x(n_x)\tau, G_y(n_y)\tau, G_z t]$, where n_x and n_y indicate that the gradient strengths are stepped in consecutive scans. The signal is described by

$$F(\mathbf{k}) = \int f(\mathbf{r})\, R(\mathbf{r}, t, \tau_m) \exp(-i\mathbf{k}\cdot\mathbf{r})\, d\mathbf{r}, \qquad [1]$$

where

$$f(\mathbf{r}) = A(\theta(\mathbf{r}))\rho(\mathbf{r})\xi(\mathbf{r}) \qquad [2]$$

is the signal arising from a volume element at coordinates $\mathbf{r} = (x, y, z)$, determined by the nutation angle through $A(\theta(\mathbf{r})) = \sin(\theta(\mathbf{r}))$, the spin density $\rho(\mathbf{r})$, and the coil responsiveness $\xi(\mathbf{r})$. The latter is defined as a dimensionless quantity normalized over the sample volume accounting for the modulus of the signal induced in the coil by a unit magnetic dipole moment situated at coordinates $\mathbf{r}$. If the same coil is used for the transmitter and receiver, the coil responsiveness $\xi(\mathbf{r})$ should be directly proportional to the $B_1(\mathbf{r})$ distribution by reciprocity (*13*), but we shall describe the most general case with separate transmitter and receiver coils. Relaxation described by the function $R(\mathbf{r}, t, \tau_m)$ will be considered to be negligible (*vide*

1090-7807/99 $30.00
Copyright © 1999 by Academic Press
All rights of reproduction in any form reserved.

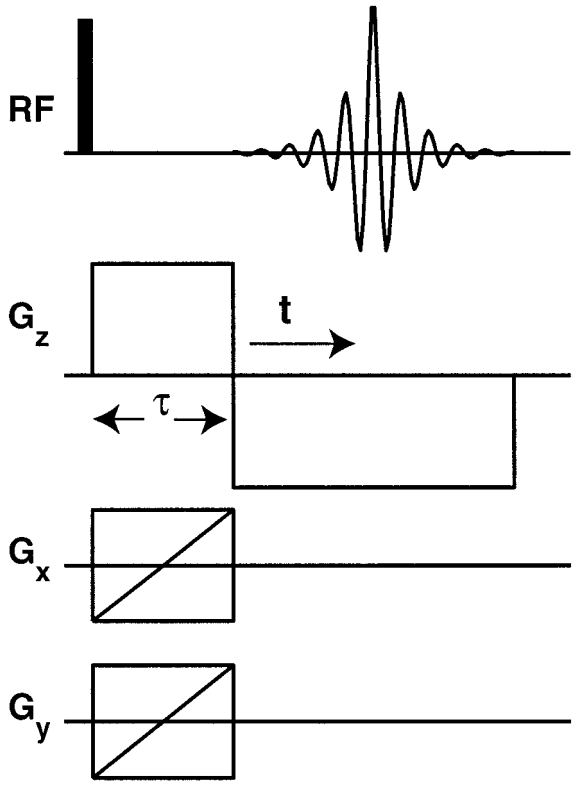

FIG. 1. Basic pulse sequence for the acquisition of a 3D image. The transverse gradients, which must be incremented in steps, are represented by rectangles with sloping ramps.

infra). The relation between the nutation angle and the B_1 field is simply $\theta(\mathbf{r}) = \gamma B_1(\mathbf{r})\delta$, where δ is the pulse duration.

For the time being, we shall assume that the gradients $G_{x,y,z}$ of the static field B_0 are linear in all three orthogonal directions. To emphasize this assumption we will refer to x, y, and z, as the *apparent* spatial coordinates, as will become clear below. A three-dimensional Fourier transform of Eq. [1] with respect to $\mathbf{k}$ yields the function $f(\mathbf{r})$ of Eq. [2]. Note that in the simple experiment of Fig. 1, the spatial dependence on the nutation angle $A = \sin(\theta(\mathbf{r}))$ cannot be separated from the coil responsiveness factor $\xi(\mathbf{r})$, nor from the spin density $\rho(\mathbf{r})$.

Figure 2 shows a distribution $f(\mathbf{r})$ for a homogeneous sample ($\rho(\mathbf{r}) = 1$) consisting of doped water in a regular 5-mm outer diameter tube, determined with the sequence of Fig. 1 and plotted as a function of the apparent variables x and z. A similar picture can be obtained when plotting $f(\mathbf{r})$ as a function of the apparent variables y and z. In Fig. 2, the intensity appears to rise toward the edges of the observed sample volume. It is unlikely that this can be attributed either to the B_1 field distribution or the responsiveness function $\xi(\mathbf{r})$. Indeed, such images were observed before in connection with gradient nonlinearity (*14*). Diffusion edge enhancement (*15*, *16*) is not an issue here, since (a) the extension of the sample in the z direction is limited only by the fading out of the B_1 field and of $\xi(z)$, and (b) edge effects in the x and y dimensions would arise only very close to the tube wall at a scale that cannot be resolved in our experiments. Likewise, diffusion in and out of the active volume is negligible with the sample dimensions and the experimental parameters used. Convection currents (*17*, *18*) can be safely ignored since the experiment was conducted at room temperature without heating.

Figure 3 shows a variant of an experiment due to Akoka *et al.* (*19*), which allows the mapping of the B_1 distribution independently of the spin density $\rho(\mathbf{r})$, independently of $\xi(\mathbf{r})$ and, as we will show, independently of nonlinearities of the B_0 gradients. The pulse sequence contains two acquisition periods, which allow one to record both the spin echo (SE) and the stimulated echo (STE). The expressions for the dependence on the nutation angle can be conveniently derived by using irreducible spherical tensor operators (*20*), considering a nutation under an rf pulse of angle θ along the y axis (rf phase $\phi = 0$):

$$I_{\pm} \rightarrow I_{\pm}\cos^2\frac{\theta}{2} \mp 2^{-1/2} I_0 \sin\theta + I_{\mp}\sin^2\frac{\theta}{2}$$

$$I_0 \rightarrow 2^{-1/2} I_+ \sin\theta + I_0\cos\theta - 2^{-1/2} I_- \sin\theta. \qquad [3]$$

The coherence pathways are $\mathbf{p} = (+1, -1)$ for the spin echo and $\mathbf{p} = (+1, 0, -1)$ for the stimulated echo. The time-domain spin echo (SE) signal $F_{\mathrm{SE}}(\mathbf{k})$ yields upon Fourier transform $f_{\mathrm{SE}}(\mathbf{r}) = A_{\mathrm{SE}}(\theta(\mathbf{r}))\rho(\mathbf{r})\xi(\mathbf{r})$ with

$$A_{\mathrm{SE}}(\theta(\mathbf{r})) = 2^{-1/2}\sin^3\theta(\mathbf{r}). \qquad [4]$$

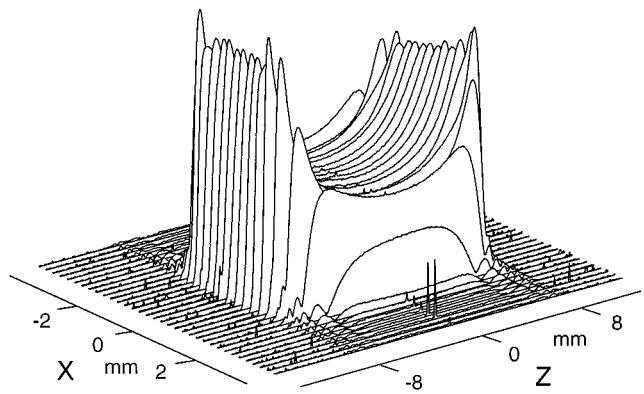

FIG. 2. Image obtained using the sequence of Fig. 1 with a doped water sample (90% H_2O and 10% D_2O) on a Bruker Avance 300 MHz spectrometer equipped with Acustar triple axes gradient amplifiers and a multinuclear 5-mm TXI probe with three self-shielded gradient coils. The image is shown as a function of the apparent x and z coordinates. A similar picture is obtained when shown as a function of y and z. The x dimension extends over 4.2 mm (inner diameter of a 5 mm sample tube) and the z-dimension over about 15 mm (active volume determined by the receiver coil response.). The nutation angle of the initial rf pulse was 45°, the relaxation delay between subsequent experiments was 20 s, $\tau = 2$ ms, $G_z = 0.035$ T/m. The transverse gradients G_x and G_y were stepped in regular increments from -0.025 to $+0.025$ T/m. The acquisition time for one scan was 8.6 ms; $64 \times 64 \times 1024$ data points were recorded in 23 h.

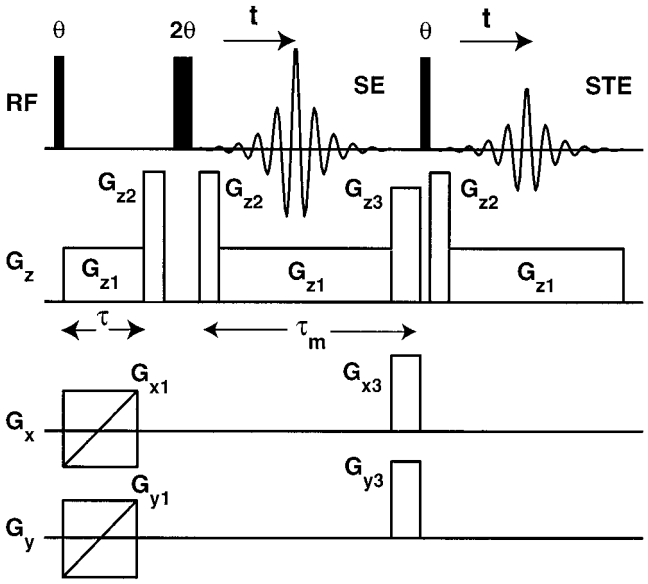

FIG. 3. Sequence for B_1 inhomogeneity mapping with acquisition of a spin-echo (SE) and a stimulated echo (STE) in intervals of equal duration (τ_m = 14.1 ms in our experiments). Typical gradient amplitudes used were G_{z1} = 0.035 T/m (τ = 2 ms), G_{z2} = 0.21 T/m (during 1.5 ms). The latter causes a dephasing of the free induction decays generated by the second and third pulses, which are strong compared to the wanted signal for extreme values of the phase encoding gradients. The G_{z3}, G_{x3}, G_{y3} gradients (typically 0.1 T/m during 4 ms) allow one to dephase unwanted stimulated echoes. The remaining parameters were the same as in Fig. 2. For the one-dimensional experiment, no phase encoding transverse gradients were used and therefore the G_{z2} gradients were not needed (this also limits errors due to diffusion in the quantitative analysis).

Likewise, the time-domain stimulated echo (STE) signal $F_{\mathrm{STE}}(\mathbf{k})$ yields $f_{\mathrm{STE}}(\mathbf{r}) = A_{\mathrm{STE}}(\theta(\mathbf{r}))\rho(\mathbf{r})\xi(\mathbf{r})$ with

$$A_{\mathrm{STE}}(\theta(\mathbf{r})) = 2^{-1/2}\sin^3\theta(\mathbf{r})\cos\theta(\mathbf{r}). \qquad [5]$$

To facilitate the comparison, the variable t represents the delay from the start of signal acquisition for both SE and STE.

To suppress three possibly interfering echoes arising at the times $t = \tau_m + m\tau$ ($m = -1, 0, 1$) after the third pulse (*21*) which stem from the pathways $\mathbf{p} = (1, m, -1)$, we applied strong spoiling gradients (G_{z3}, G_{x3}, and G_{y3} in Fig. 3) after the acquisition of the spin echo to dephase transverse magnetization ($p \neq 0$) at the end of the τ_m interval. Gradients along different axes help to avoid accidental refocusing. Additional gradients, G_{z2}, were used to remove unwanted free induction decays excited by the second and third pulses.

The spatial dependence of the nutation angle can be obtained from the ratio

$$\theta(\mathbf{r}) = \mathrm{acos}\left(\frac{f_{\mathrm{STE}}(\mathbf{r})}{f_{\mathrm{SE}}(\mathbf{r})}\right). \qquad [6]$$

The function of Eq. [6] is independent of both spin density $\rho(\mathbf{r})$ and coil responsiveness $\xi(\mathbf{r})$. In addition, phase errors from rf offsets, inaccuracies of the gradient areas, and effects of transverse relaxation are canceled. Thus the θ distribution of Eq. [6] can be obtained without need for any phase correction.

It may be further safely assumed that $\tau_m \ll T_1$, since τ_m is on the order of milliseconds, so that longitudinal relaxation does not affect the result.

RESULTS AND DISCUSSION

Figure 4 shows (a) the spin-echo part, (b) the stimulated echo part, and (c) the B_1 field map (θ map) obtained by the procedure outlined above as a function of the (apparent) z and x coordinates. An equivalent picture can be obtained as a function of the z and y coordinates.

From the B_1 distribution and the magnitude of the spin-echo signal we can calculate the distribution of the product $\rho(\mathbf{r})\xi(\mathbf{r})$ using

$$\rho(\mathbf{r})\xi(\mathbf{r}) \propto \frac{|f_{\mathrm{SE}}(\mathbf{r})|}{\sin^3\theta(\mathbf{r})}. \qquad [7]$$

Since $\rho(\mathbf{r})$ is uniform for a homogeneous sample, Eq. [7] yields $\xi(\mathbf{r})$ directly (apart from a constant factor).

Figures 5a and 5b show one-dimensional images as a function of the apparent z coordinate derived from the spin echo and stimulated echo signals acquired with a one-dimensional version of the experiment of Fig. 3 (in this case the gradients G_{x1}, G_{y1}, and G_{z2} were not used, as explained in the caption). All images are represented in absolute value. Figure 5c shows the θ distribution calculated using Eq. [6], and Fig. 5d shows the ξ distribution calculated using Eq. [7]. It seems surprising that the ξ distribution is not proportional to the θ distribution (Figs. 5c and 5d), as would be expected from the reciprocity relation (*13*) if the same coil were used for transmitting and receiving. Again, the coil response appears to rise toward the edges, which is a symptom of nonlinearities of the B_0 gradients (*14*). The B_1 field is fairly uniform along the x and y directions, but severe inhomogeneities are found in the z direction as can be seen in Fig. 4c. We shall therefore restrict the treatment of nonlinear B_0 gradients to one-dimensional images along the z direction.

The signal acquired in the presence of a gradient applied along the z dimension is described by

$$F(k) = \int f(z)\exp(-ikz)dz, \qquad [8]$$

where $k = \gamma Gt$, $f(z) = A(\theta(z))\rho(z)\xi(z)$, and where relaxation is ignored. $F(k)$ and $f(z)$ form a Fourier pair if the gradients are linear. If the gradients are nonlinear the spatial function $\tilde{k}(\tilde{z}) = \gamma G(\tilde{z})t$ depends on the true spatial coordinate $\tilde{z}$. The signal is then described by

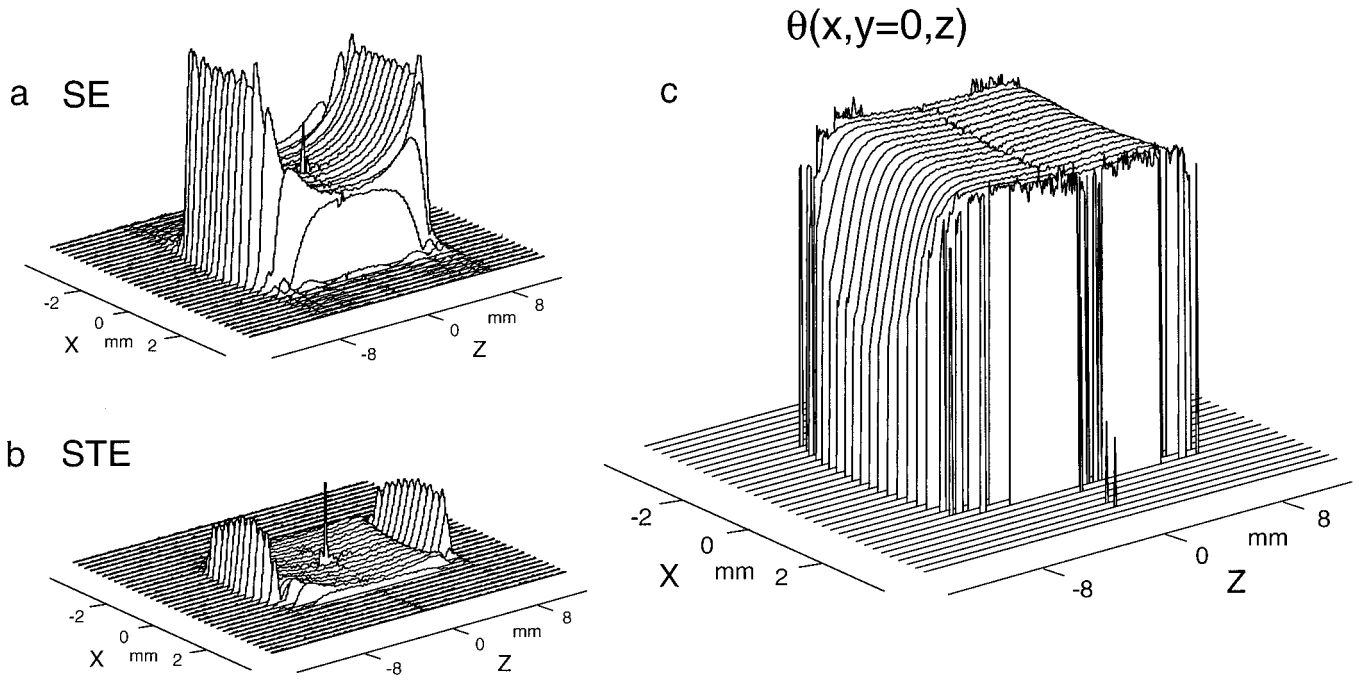

FIG. 4. Two-dimensional images derived from the (a) spin echo and (b) stimulated echo signals acquired with the three-dimensional experiment of Fig. 3, shown as a function of the apparent x and z coordinates, corresponding to a section (thickness 0.2 mm) through the middle of the sample, i.e., centered at $y = 0$. (c) Spatial distribution of the nutation angle θ (which is proportional to the B_1 field) obtained from (a) and (b) by using Eq. [6]. The images are presented in absolute value. A threshold value was used in the calculation of Eq. [6] in order to avoid singularities.

$$F(k) = \int \tilde{f}(\tilde{z}) \exp[-i\tilde{k}(\tilde{z})\tilde{z}]d\tilde{z}, \qquad [9]$$

where $\tilde{f}(\tilde{z})$ is the true image as a function of the true (undistorted) spatial coordinate $\tilde{z}$. The relationship between the apparent spatial coordinate z and the true coordinate $\tilde{z}$ is defined by a mapping function $u(\tilde{z})$:

$$z = u(\tilde{z}) = \frac{\tilde{k}(\tilde{z})\tilde{z}}{k}. \qquad [10]$$

Using $dz = u'(\tilde{z})d\tilde{z}$ and $\tilde{z} = u^{-1}(z)$, Eq. [9] can be rewritten in the form

$$F(k) = \int \frac{\tilde{f}(u^{-1}(z))}{u'(u^{-1}(z))} \exp(-ikz)dz. \qquad [11]$$

By comparing this with Eq. [8] we find that

$$f(z) = \frac{\tilde{f}(u^{-1}(z))}{u'(u^{-1}(z))}, \qquad [12]$$

which is the information we are looking for. These equations may be seen as generalizations of the Fourier shift theorem (*22*). The above treatment is only valid if $u'(\tilde{z})$ exists and if $u^{-1}(z)$ is uniquely defined, i.e., $\tilde{k}(\tilde{z})$ should be a smooth and strictly monotonic function. These conditions are usually met in practical situations.

As may be appreciated from the above discussion, Figs. 5c and 5d represent the distorted functions $\xi(z)$ and $\theta(z)$ of the apparent spatial coordinate z. With recourse to the reciprocity relation we assume that the true functions $\tilde{\xi}(\tilde{z})$ and $\tilde{\theta}(\tilde{z})$ are proportional to each other, from which we deduce through Eq. [12] and the fact that the awkward term $u'(u^{-1}(z))$ drops out when deriving θ from Eq. [6] that

$$\frac{\theta(z)}{\xi(z)} \propto u'(\tilde{z}) \qquad [13]$$

and we obtain

$$\tilde{z} = u^{-1}(z) = \int_a^z \frac{\delta\tilde{z}}{\delta z} dz$$

$$= \int_a^z \frac{1}{u'(u^{-1}(z))} dz \propto \int_a^z \frac{\xi(z)}{\theta(z)} dz, \qquad [14]$$

which allows us to calculate the function $\tilde{z} = u^{-1}(z)$ of Fig. 5e. (For convenience the same symbol z was used for the integration variable and its upper bound, and a denotes a

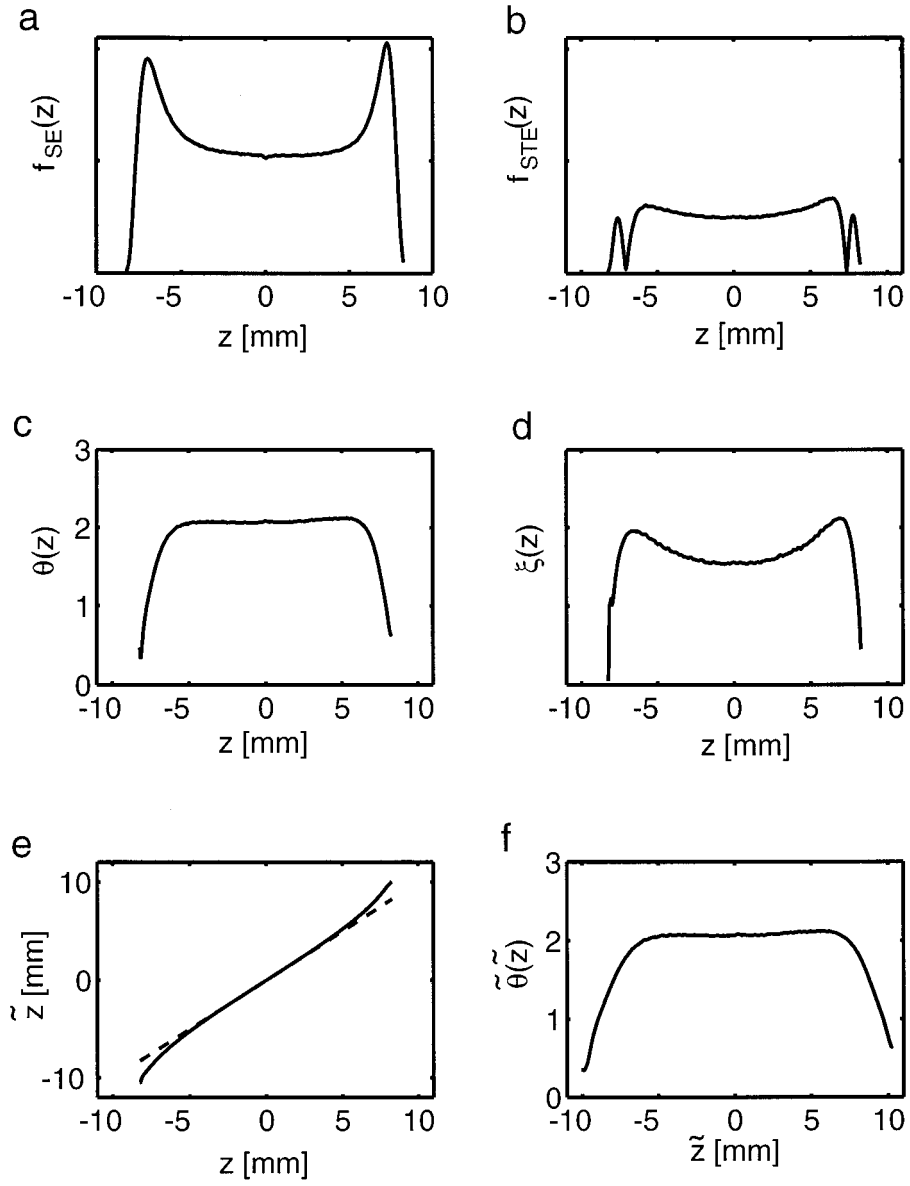

FIG. 5. One-dimensional images derived from (a) spin echo and (b) stimulated echo signals acquired with a one-dimensional version of the experiment of Fig. 3 ($G_{z1} = 0.07$ T/m, but G_{z2} and the associated delays were removed). Five hundred twelve points were acquired during 4.3 ms, and $\tau_m = 8.3$ ms. All images are presented in absolute value. The variable $\tilde{z}$ represents the true (vertical) coordinate, while z is the apparent coordinate observed if one does not correct for the nonlinearity of the G_z gradient. (c) Apparent θ distribution (in radians) calculated from (a) and (b) using Eq. [6]. (d) Apparent ξ distribution calculated from (a) and (c) using Eq. [7]. The undistorted variable $\tilde{z} = u^{-1}(z)$ represented in (e) is obtained from (c) and (d) by using Eq. [14], which is then used to remap (c) to give the undistorted θ distribution (radians) represented in (f). The homogeneous region of the B_1 field extends over about 1.6 cm, which approximately matches the active volume defined by the rf coil. The apparent coordinate was calibrated by confining the sample volume and measuring the height in Hz. The z gradient was fairly linear over a region of 5.5 mm in the center of the active volume, as was verified thereafter in (e). A threshold value was used in the calculation of Eq. [6] in order to avoid singularities.

reference point to obtain the correct constant offset after integration.) This function relates the apparent spatial coordinate to the true coordinate. Using this function we can obtain the correct nutation angle distribution, which in this case amounts to "stretching" the regions near the edge of the sample (Fig. 5f). This function may also be obtained without taking recourse to the reciprocity relation by iterative fitting of the experimental data assuming a uniform B_1 field in the central region. This can be useful if a B_1 profile must be obtained with different coils for rf transmission and signal acquisition.

Figure 5f shows that in the probe under investigation, the largest B_1 inhomogeneities occur near the edges of the active volume in the z direction. Obviously, this region accounts for most of the rf pulse imperfections. It is possible to reduce the troublesome edge region by using susceptibility-matched plugs to restrict the sample to the region where the B_1 fields are

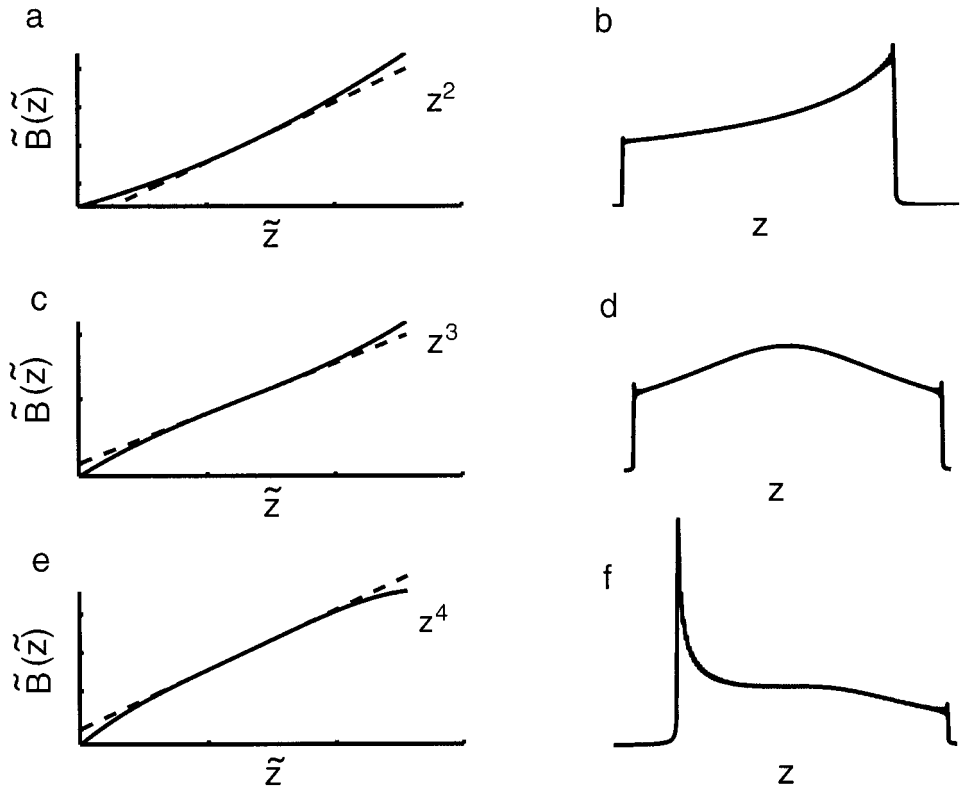

FIG. 6. Effects of nonlinearity of the B_0 gradients on the appearance of one-dimensional images, assuming uniform excitation and uniform spin density. In these simulations, the deviations from linearity of the field produced by the gradients were assumed to be proportional to (a,b) $\tilde{z}^2$, (c,d) $\tilde{z}^3$, (e,f) $\tilde{z}^4$. The sharp features at the edges of the profiles are due to truncation errors (no window functions were used).

uniform. Many effects of pulse imperfections should then be eliminated. It may be possible to reduce excessively long phase cycles, one of the main effects of which may well be the elimination of artifacts stemming from the edge regions. The confinement of the sample volume may also reduce convection currents (*17, 18*).

Figure 6 illustrates the effects expected for various nonlinearities of the gradients, assuming quadratic, cubic, and quartic dependencies on the spatial coordinates.

Figure 7 demonstrates transverse magnetization profiles simulated for pulses with nominal nutation angles $m\pi$. When the rf pulses are long, the magnetization near the edges experiences oscillations as a function of the spatial coordinates, while the magnetization in the central region remains fairly uniform. It should be mentioned that the usual experimental criterion for the calibration of $m\pi$ pulses is the nulling of the signal integral. In actual fact, substantial transverse magnetization with alternating signs remains in different parts of the sample. This is why a residual signal is often seen after the application of $m\pi$ pulses. Residual B_0 inhomogeneity may draw the regions with positive and negative signals apart so that they do not cancel. It is obvious that if the edge regions are removed by restricting the sample volume the criterion of signal nulling would be more meaningful and pulse calibration would be more accurate.

Magnetization profiles such as in Fig. 7 cannot easily be measured experimentally. Imaging methods normally do not provide the sign of the magnetization. The method of Fig. 3 and Eq. [6] was found to be unstable for nutation angles θ larger than 90°. Besides, singularities arise near zero-crossings.

Detailed information about the active volume as defined by the responsiveness $\xi(\mathbf{r})$ of the receiver coil and the B_1 distribution may be useful for the study of diffusion, flow, and convection, especially in the edge region. Flow in and out of the active volume may be particularly important at elevated temperatures (*17, 18*). The strength of the B_1 gradient that we have determined in the edge region is approximately 0.3 T/m, which is of the same order of magnitude as the B_0 gradients (0.6 T/m) that are available in modern high-resolution probes. Probes of an older design may have even larger B_1 gradients. Thus it may be possible to measure diffusion coefficients using B_1 gradients in standard high-resolution probes.

CONCLUSIONS

We have shown how B_1 field maps can be obtained independently of spin density, coil responsiveness, and gradient nonlinearities. In the high-resolution probe used in this investigation, the rf field gradients in the x and y directions were found to be negligible compared to those in the z direction, and the largest inhomogeneities are found (not surprisingly) at the edges of the active volume. This study indicates that the use of

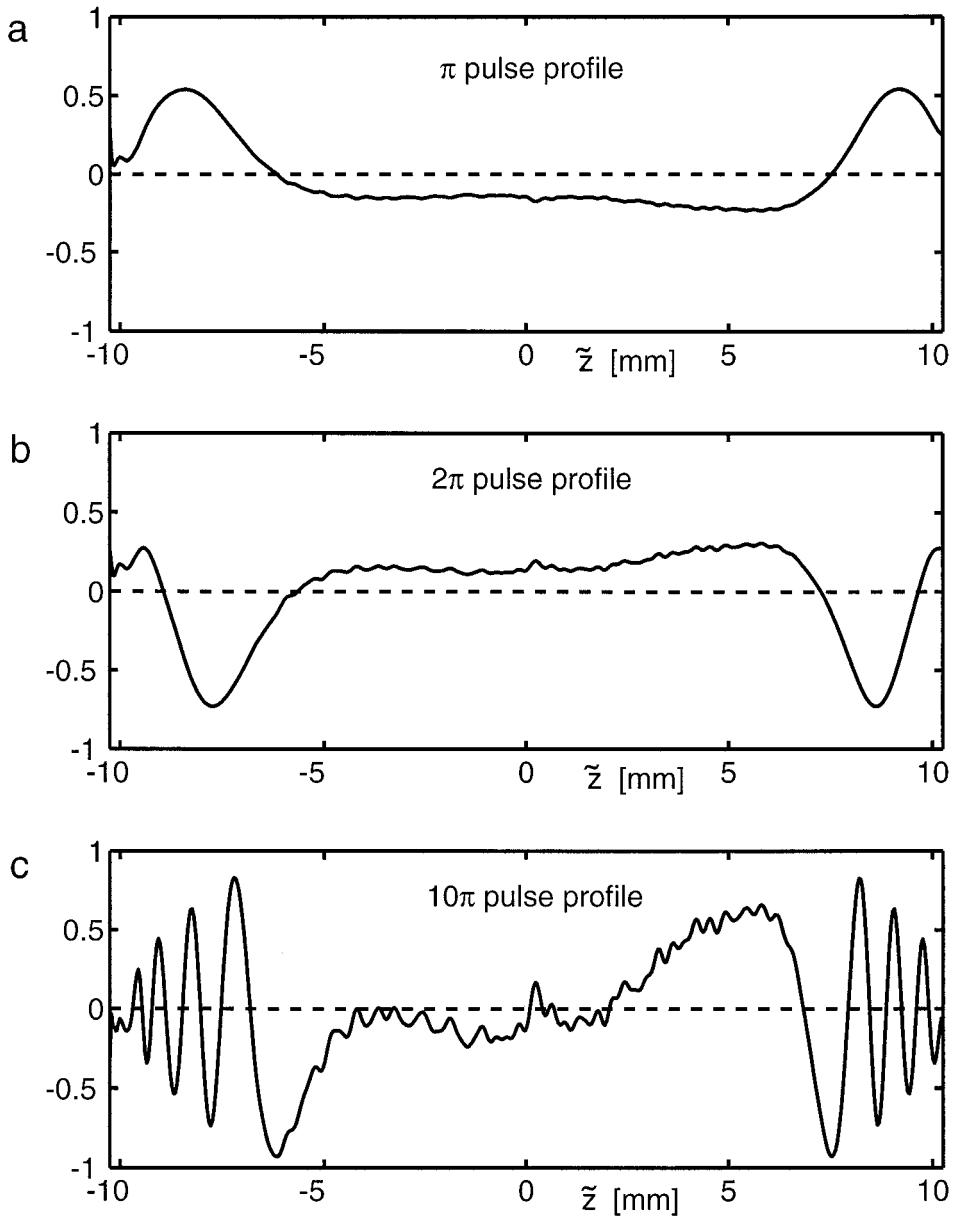

FIG. 7. Distributions of the transverse magnetization M_x simulated using the experimentally determined distribution of the B_1 field (see Fig. 5f.) The distribution of M_x is calculated after rf pulses with different nominal nutation angles: (a) π, (b) 2π, and (c) 10π. A pulse with a "nominal" nutation angle $m\pi$ is defined by the demand that the integral of M_x over the entire sample must vanish. This is the usual criterion for calibrating rf pulses experimentally. In actual fact, even if the net magnetization vanishes, there is a significant fraction of the magnetization which experiences shorter nutation angles, particularly near the edges of the active volume.

susceptibility-matched plugs to restrict the sample volume should greatly improve the performance of many experiments. As a by-product we have obtained a map of the (nonlinear) B_0 fields produced by the gradients. The quantitative information thus obtained is useful in detailed studies of the effects of B_1 inhomogeneities in NMR pulse sequences.

ACKNOWLEDGMENTS

This work was supported by the Fonds National de la Recherche Scientifique (FNRS) and by the Commission pour la Technologie et l'Innovation (CTI) of Switzerland.

REFERENCES

1. Y. Zhang, W. E. Maas, and D. G. Cory, Analysis of homonuclear RF gradient NMR spectroscopy, *Mol. Phys.* **86,** 347 (1995).
2. G. Otting, Improved resolution and sensitivity in NOE and ROE experiments with water by the use of B_1 gradients, *J. Magn. Reson. B* **103,** 288 (1994).
3. K. Woelk, R. E. Gerald II, R. J. Klingler, and J. W. Rathke, Imaging diffusion in toroid cavity probes, *J. Magn. Reson. A* **121,** 74 (1996).
4. R. Kimmich, B. Simon, and H. Köstler, Magnetization-grid rotating frame imaging technique for diffusion and flow measurements, *J. Magn. Reson. A* **112,** 7 (1995).

5. M. Valtier, R. Raulet, R.-P. Eustache, and D. Canet, Spectral selectivity in imaging by radiofrequency field gradients, *J. Magn. Reson. A* **112,** 118 (1995).
6. F. Humbert, B. Diter, and D. Canet, NMR microscopy by strong radiofrequency-field gradients with spatial resolution better than five micrometers, *J. Magn. Reson. A* **123,** 242 (1996).
7. D. I. Hoult, Rotating frame zeugmatography, *J. Magn. Reson.* **33,** 183 (1979).
8. E. Mischler, F. Humbert, and D. Canet, A one-shot diffusion sequence using a B_1 gradient, *J. Magn. Reson. B* **109,** 121 (1995).
9. E. Mischler, F. Humbert, B. Diter, and D. Canet, Measurement of one-dimensional spatially resolved self-diffusion coefficients and longitudinal relaxation times with a single B_1 gradient, *J. Magn. Reson. B* **106,** 32 (1995).
10. D. Canet, Radiofrequency field gradient experiments, *Prog. Nucl. Magn. Reson.* **30,** 101 (1997).
11. E. Chiarparin, P. Pelupessy, and G. Bodenhausen, Selective cross polarization in solution-state NMR, *Mol. Phys.,* in press.
12. P. T. Callaghan, "Principles of Nuclear Magnetic Resonance Microscopy," Oxford University Press (1993).
13. D. I. Hoult and R. E. Richards, The signal-to-noise ratio of the nuclear magnetic resonance experiment, *J. Magn. Reson.* **24,** 71 (1976).
14. R. E. Hurd, A. Deese, M. O'Neil Johnson, S. Sukumar, and P. C. M. van Zijl, Impact of differential linearity in gradient enhanced NMR, *J. Magn. Reson. A* **119,** 285 (1996).
15. P. T. Callaghan, A. Coy, L. C. Forde, and C. J. Rofe, Diffusive relaxation and edge enhancement in NMR microscopy, *J. Magn. Reson. A* **101,** 347 (1993).
16. T. M. de Swiet, Diffusive edge enhancement in imaging, *J. Magn. Reson. B* **109,** 12 (1995).
17. A. Jerschow and N. Müller, Suppression of convection artifacts in stimulated echo diffusion experiments: Double stimulated echo experiments, *J. Magn. Reson.* **125,** 372 (1997).
18. A. Jerschow and N. Müller, Convection compensation in gradient enhanced nuclear magnetic resonance spectroscopy, *J. Magn. Reson.* **132,** 13 (1998).
19. S. Akoka, F. Franconi, F. Seguin, and A. Le Pape, Radiofrequency map of an NMR coil by imaging, *Magn. Reson. Imag.* **11,** 437 (1993).
20. M. E. Rose, "Elementary Theory of Angular Momentum," Wiley, New York (1966).
21. J. W. Carlson and D. M. Kramer, Rapid radiofrequency calibration in MRI, *Magn. Reson. Med.* **15,** 438 (1990).
22. D. C. Champeney, "A Handbook of Fourier Theorems," Cambridge Univ. Press, Cambridge, UK (1990).